PHYSICAL REVIEW B **109**, 085409 (2024)

Band engineering of phosphorene/graphene van der Waals nanoribbons toward high-efficiency thermoelectric devices

Maryam Mahdavifar,[1] Farhad Khoeini,[1,*] and Francois M. Peeters[2,3]

[1]Department of Physics, University of Zanjan, P.O. Box 45195-313, Zanjan, Iran
[2]Centre for Quantum Metamaterials, HSE University, Moscow 101000, Russia
[3]Departamento de Física, Universidade Federal do Ceará, Fortaleza, Ceará 60455-760, Brazil

(Received 3 December 2023; accepted 22 January 2024; published 12 February 2024)

Vertical integration of dissimilar layered materials in a so-called van der Waals (vdW) heterostructure (HS) has emerged as a useful tool to engineer band alignments and interfaces. In this paper, we investigate thermoelectric currents in a phosphorene/graphene vdW nanoribbon consisting of an armchair graphene nanoribbon (AGNR) stacked on an armchair phosphorene nanoribbon (APNR). We focus on the currents driven by a temperature difference between the leads in a two-probe junction. In contrast to pristine AGNRs and APNRs, such an armchair-edged HS can provide several nanoamperes of the current at room temperature, without any external field. External electric fields modify the electronic band structure and can induce a type I-to-II band alignment transition and a direct-to-indirect band gap transition. Biasing the APNR/AGNR by an external electric field is found to strongly increase the thermally induced current and control the direction of current flow at moderate temperatures. These results are important for potential applications of the APNR/AGNR vdW HS in flexible electronics and thermoelectric devices.

DOI: 10.1103/PhysRevB.109.085409

I. INTRODUCTION

Two-dimensional (2D) nanomaterials have been recognized as potential candidates for next-generation electronics because of their exotic electrical, mechanical, optical, and thermal properties, which are not revealed in their bulk counterparts [1–6]. Among the family of 2D layered structures, graphene has emerged as the most appealing material in the last two decades. Graphene is defined as a single layer of sp^2-hybridized carbon atoms packed into a honeycomb structure, which has been demonstrated to host intriguing electronic and quantum transport properties, such as massless Dirac fermions, high charge carrier mobility, and half-integer quantum Hall effect [7–10]. However, the gapless nature of this key material reduces its utility for practical applications [10,11]. Hence, many efforts have been dedicated to create a small electronic band gap in graphene, e.g., involving the size effect [12–15].

The isolation of graphene by mechanical exfoliation of graphite [1] brought forth a significant advancement of thin-layer processing methods, giving rise to renewed research interest in graphitelike layered materials such as black phosphorus (BP) [16,17]. BP, the most thermodynamically stable allotrope of phosphorus [18–20], is made of single-atom-thick sheets which are held on top of each other by weak van der Waals (vdW) forces [21,22]. Due to the weak forces of attraction between layers, few-layer BP, known as phosphorene, can be easily cleaved from bulk crystals [4]. Due to the sp^3 hybridization of phosphorus atoms, it has a hexagonal arrangement with a puckered structure, resulting in an in-plane anisotropic spectrum [23,24]. As a semiconductor, it exhibits a nearly direct band gap, which is strongly thickness dependent, increasing from $\sim$0.3 to $\sim$2 eV with decreasing thickness [25–27]. Moreover, it shows interesting properties, including a high carrier mobility of $\sim 1000\,\text{cm}^2\,\text{V}^{-1}\,\text{s}^{-1}$, a moderate on/off current ratio of $\sim 10^4$, and negative reflection [4,28,29]. With its lower effective masses of carriers than transition metal dichalcogenides [25,30], phosphorene is more suitable for engineering devices. Despite these extraordinary properties, a main issue hindering phosphorene application in electronic devices is its poor air stability [31,32].

Integrating dissimilar 2D materials in a so-called vdW heterostructure (HS) is a useful tool to engineer band alignments [33–35]. Compared with single-material systems, HSs seem to be more promising for functional material applications due to the possibility of electronic band engineering. Along with the rapid development of vdW HSs, several different types of phosphorene-based HSs have been recently studied in detail and utilized in electronic devices, e.g., the vdW phosphorene/graphene Schottky junction [36], the phosphorene/MoS_2 junction as an effective solar cell material [37], and phosphorene-based field-effect transistors [38,39]. Interestingly, an HS constructed with a proper layer-by-layer assembly not only may serve to overcome the intrinsic shortcomings of the materials but also provide functionalities such that the relevant properties of each component material can be effectively maintained. For instance, to protect phosphorene from structural and chemical degradation, a graphene layer or a hexagonal boron nitride layer has been proposed to be stacked on top of it, preserving the distinctive features of phosphorene [40]. The HSs have also received significant attention

*khoeini@znu.ac.ir

 ©2024 American Physical Society

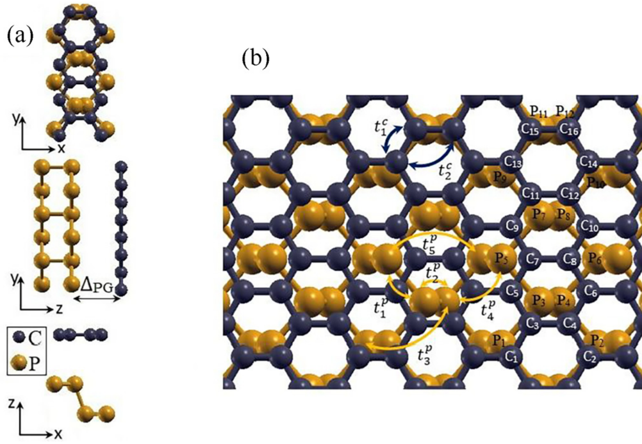

FIG. 1. (a) Different views of the supercell of phosphorene/graphene van der Waals (vdW) heterostructure (HS) consisting of a 1×4 monolayer graphene supercell stacked on top of a 1×3 monolayer phosphorene supercell. (b) Schematic of two-dimensional (2D) HS. Black lattice is graphene and the orange one is phosphorene. The atomic sites are labeled per supercell, and the different hopping parameters are indicated.

in designing high-performance thermoelectric devices. Zeng *et al.* [41] predicted a significant enhancement in the thermally induced current of an H-terminated zigzag graphene ribbon (ZGNR) contacted to an O-terminated ZGNR compared with a perfect H-terminated ZGNR. Hu *et al.* [42] reported an enhancement in the *ZT* value of BP/blue phosphorus vdW HS compared with pristine layers.

In this paper, we investigate current driven by a temperature difference in an armchair phosphorene nanoribbon (APNR) stacked on an armchair graphene nanoribbon (AGNR) by solving the electronic transmission in the nonequilibrium Green's function formalism. We use the tight-binding (TB) model to describe the electronic structure of the system. It was reported that APNRs [43] and AGNRs [44] show excellent thermoelectric performance by gating or doping. Authors of a recent study have shown high thermoelectric performance in a phosphorene nanoring contacted to an APNR with modulation of the chemical potential [45]. Unlike pure APNRs and AGNRs, an APNR/AGNR vdW HS is found to offer several nanoamperes of thermally induced current at moderate temperatures, without the presence of any field. We also investigate the effect of external electric fields on the thermally induced current, which revealed a significant enhancement with electric field.

II. MODEL AND METHOD

A 2D phosphorene/graphene vdW HS consists of monolayer graphene lying on monolayer phosphorene. Since we are interested in the minimal lattice mismatch between the layers, we suppose that the unit cell of the HS is composed of a 1×4 graphene supercell stacked on top of a 1×3 monolayer phosphorene supercell, as shown in Fig. 1(a). The remaining mismatch should be compensated by strain. Due to the weak dependence of the electronic spectrum of graphene on strain [46] (unlike phosphorene [23]), it is applied only to the graphene layer. Considering the equilibrium geometry obtained from density functional theory (DFT) calculations reported in Ref. [36], the interlayer distance Δ_{PG} is assumed to be 3.45 Å.

We denote an armchair-edged phosphorene/graphene vdW HS by N_{P}APNR/N_{G}AGNR, where N_{P} and N_{G} are defined as the number of rows of atoms parallel to the x axis [Fig. 1(a)] for APNR and AGNR, respectively. For instance, the armchair-edged nanoribbon with the same width of the supercell shown in Fig. 1(a) (the periodicity is along the x axis) has a width index of $N_{\mathrm{P}} = 6$ and $N_{\mathrm{G}} = 8$, denoted by 6APNR/8AGNR, and resulting in a width (W) of ∼8.6 Å.

The low-energy Hamiltonian is described within a simplified TB model, including five hopping parameters for the phosphorene layer [47], first- and second-neighbor hopping parameters for the graphene layer [48], and a coupling parameter between two layers specified within the method introduced in Ref. [49]. We emphasize that the model is valid only at low energies. The explicit representation is given in the appendix.

In this paper, using the nonequilibrium Green's function method, we study the evolution of the thermally induced current through a two-probe junction depending on the width as well as under biasing, which is implemented by external electric fields. We set up the two-probe junction by partitioning APNR/AGNR into a central region and two semi-infinite terminations as source and drain leads. The formalism is as follows.

The Green's function of the junction is defined as [50,51]

$$\mathbf{G}(E) = [(E + \mathrm{i}\eta)\mathbf{I} - \mathbf{H} - \mathbf{\Sigma}_{\mathrm{L}}(E) - \mathbf{\Sigma}_{\mathrm{R}}(E)]^{-1}, \quad (1)$$

where η denotes an arbitrary infinitesimal number, $\mathbf{I}$ is the identity matrix, and $\mathbf{H}$ is the real-space Hamiltonian matrix. Additionally, $\mathbf{\Sigma}_{\mathrm{L}}$ ($\mathbf{\Sigma}_{\mathrm{R}}$) is the self-energy term, which can be interpreted as the effective Hamiltonian arising from the coupling of the central region with the left (right) lead. We compute the self-energies using the iterative procedure introduced in Refs. [52–54]. The electronic transmission probability [55–57] is given by

$$T_{\mathrm{e}}(E) = \mathrm{Tr}[\mathbf{\Gamma}_{\mathrm{L}}(E)\mathbf{G}(E)\mathbf{\Gamma}_{\mathrm{R}}(E)\mathbf{G}^{\dagger}(E)], \quad (2)$$

where $\mathbf{\Gamma}_{\mathrm{L}(R)}$, the broadening function of the left (right) lead, is given by

$$\mathbf{\Gamma}_{\mathrm{L(R)}}(E) = \mathrm{i}\{\mathbf{\Sigma}_{\mathrm{L(R)}} - [\mathbf{\Sigma}_{\mathrm{L(R)}}]^{\dagger}\}. \quad (3)$$

In addition, the density of states (DOS) at energy E is described as

$$\mathrm{DOS}\,(E) = -\frac{1}{\pi}\mathrm{Im}\{\mathrm{Tr}[\mathbf{G}(E)]\}. \quad (4)$$

The local DOS (LDOS) is understood as the spatial distribution of electronic states at a given energy.

The temperature difference between the leads gives rise to a current I through the contact given by

$$I(T) = 2\frac{\mathrm{e}^2}{\mathrm{h}}\int dE\; T_{\mathrm{e}}(E)[f_{\mathrm{L}}(E-\mu) - f_{\mathrm{R}}(E-\mu)], \quad (5)$$

where μ and h are the chemical potential and the Planck constant, respectively. The factor 2 accounts for the spin degeneracy. Additionally, $f_{\mathrm{L(R)}} = 1/\{1 + \exp[\frac{E-\mu}{k_{\mathrm{B}}T_{\mathrm{L(R)}}}]\}$ is the

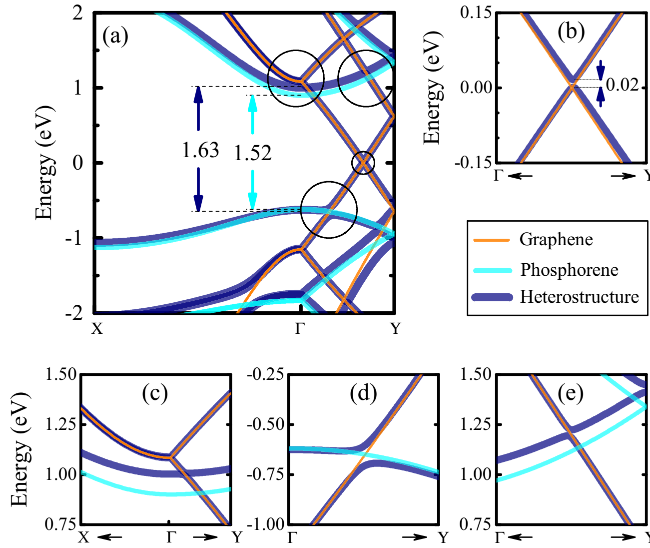

FIG. 2. (a) The band dispersion of the two-dimensional (2D) heterostructure (HS), graphene, and phosphorene. The enlarged views of the regions indicated by the black circles are shown in (b)–(e), representing (b) the Dirac cone, and (c)–(e) band anticrossings.

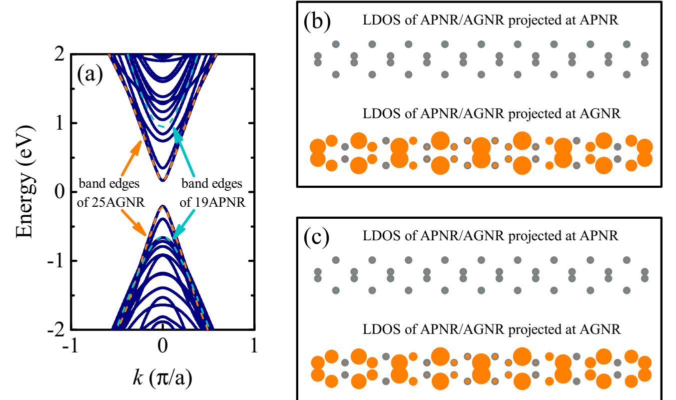

FIG. 3. (a) The band dispersion of 19APNR/25AGNR, together with the band edges of 19APNR and 25AGNR, depicted by the dashed lines. Local density of states (LDOS) of 19APNR/25AGNR at (b) conduction band minimum (CBM) and (c) valence band maximum (VBM), projected at the layers.

Fermi distribution function related to the left (right) lead at the temperature of $T_{L(R)}$, where k_B is the Boltzmann constant.

III. DISCUSSION

A. The electronic structure of 2D HS

Our approach is to use the TB model for calculating the thermally induced current in the armchair-edged HS. However, to assess the reliability of the TB parametrization, we first use the model to calculate the electronic structure of a 2D phosphorene/graphene vdW HS and compare the results with previous works based on DFT calculations. Figure 2 shows the band dispersion of the HS together with that of the pristine layers. As shown in Fig. 2(a), compared with the energy bands of the pristine layers, the superpositions of the HS are slightly perturbed. Moreover, a band gap increase of 0.11 eV is induced to phosphorene by forming the vdW HS. The enlarged views of the regions, indicated by the black circles in Fig. 2(a), representing the Dirac cone or a band anticrossing, are shown in Figs. 2(b)–2(e). Figure 2(b) reveals that the Dirac point undergoes a small splitting of ∼0.02 eV and becomes higher in energy by ∼0.01 eV upon contact. In addition, the band-cross points open a gap by <0.06 eV because of the vdW interlayer coupling. These results are in good agreement with previous DFT calculations [36,58].

B. Thermally induced current in the armchair nanoribbon

In this section, we focus on the electronic currents resulting from a temperature difference between the leads of a two-probe junction with armchair edges without any biasing. To determine the electronic properties of the armchair-edged HS, we first investigate the electronic structure and transmission coefficients of APNR/AGNR.

All APNRs exhibit semiconducting character, with an energy gap >1.56 eV for W < 4 nm [59]. As a result of the symmetry restrictions, the three characteristic groups of AGNR are defined by the width rule (semiconducting for $N_{\mathrm{Gr}} = 3n,\ 3n+1$ and metallic for $N_{\mathrm{Gr}} = 3n+2$, where $n = 1,\ 2,\ 3,\ldots$) [12]. Hence, we have two possible electronic configurations for the APNR/AGNR interface depending on the width: semiconductor/semiconductor or semiconductor/metal. For instance, the band structure of 19APNR/25AGNR (a semiconductor/semiconductor junction) and its spatial electronic state distribution per supercell at the conduction band minimum (CBM) and valance band maximum (VBM), projected at the component layers, are shown in Figs. 3(a)–3(c), respectively. Within the TB model, 19APNR shows a band gap of 1.590 eV, while 25AGNR has a narrow gap of 0.379 eV. The band edges of pristine layers are also shown by the dashed lines in Fig. 3(a), which reveals a type-I band alignment for 19APNR/25AGNR. In this case, the CBM and VBM lie in the graphene layer, which is also seen in Figs. 3(b) and 3(c). Hence, it is expected that 19APNR/25AGNR inherits the electronic properties of 25AGNR at the band edge extrema. However, the coupling between the p_z orbitals of APNR and the π cloud of AGNR results in a band offset and a small decrease in the band gap (0.009 eV) upon binding.

Considering the three characteristic groups of AGNR, we take the cases of 18APNR/24AGNR and 19APNR/25AGNR as examples of the semiconductor/semiconductor junction and 20APNR/26AGNR as an example of the semiconductor/metal one. The electron transmission of 18APNR/24AGNR, 19APNR/25AGNR, and 20APNR/26AGNR are shown in Figs. 4(a)–4(c), respectively. The dashed lines plotted in Figs. 4(a)–4(c) exhibit the range at which the distribution function is broadened at room temperature which, for illustration purposes, we took $|E - E_F| < 10\ k_B T_L$ (where E_F is the Fermi level). From the expression of current defined by Eq. (5), the only charge carriers which can participate in the current have energy within the range $|E - E_F| < 10\ k_B T_L$. The charge carriers with energy higher than the Fermi energy contribute to the electron current (I_e), and those with energy lower than the Fermi energy contribute to the hole

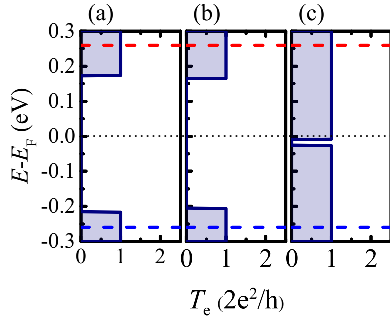

FIG. 4. The electron transmission of (a) 18APNR/24AGNR, (b) 19APNR/25AGNR, and (c) 20APNR/26AGNR, as a function of energy.

current (I_h). Considering the compensation effect (also reported in Refs. [41,60]), the more I_e overcomes I_h, the larger the thermally induced current, which indicates that the current should be dominated by the net transmission within the range $|E - E_F| < 10\ k_B T_L$. The thermally induced current vanishes in perfect AGNRs, arising from the symmetric transmission spectrum around the Fermi level. Although the transmission spectrum of APNRs is asymmetrical [61], it is not possible to induce a current at moderate temperature due to the presence of a relatively large gap. Indeed, the distribution function must be broadened by a significantly large temperature to generate a current in APNRs, which reduces its utility in practical applications. The nonsymmetric transmission spectrum of the heterojunction is due to the different symmetries of the wave functions in the component layers [62], which can offer a nonzero current.

Figure 5 represents the current against the width of the HS at $T_L = 300$ K for $\Delta T = 10,\ 20,$ and 30 K. The widths denoted by (a)–(c) correspond to Figs. 4(a)–4(c). According to Fig. 4(c), attributed to a semiconductor/metal heterojunction ($W_G = 3n + 2$), within the specified range, the transmission is close to $2e^2/h$ when the charge carriers have energy higher than E_F, whereas a small gap of $\sim$0.02 eV is seen when the charge carriers have energy lower than E_F. Therefore, the electron current dominates over the hole current, which results in several nanoamperes of thermally induced current for various

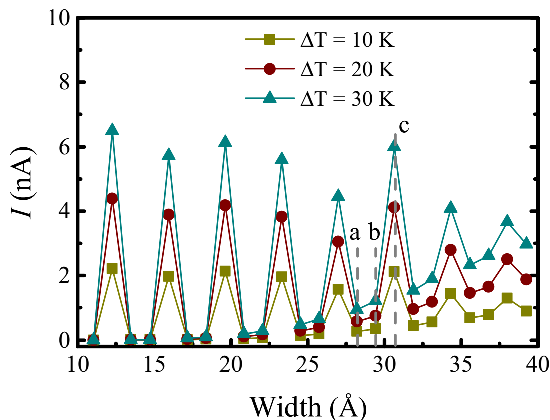

FIG. 5. The thermally induced current against the width of the heterostructure (HS) at $T_L = 300$ K.

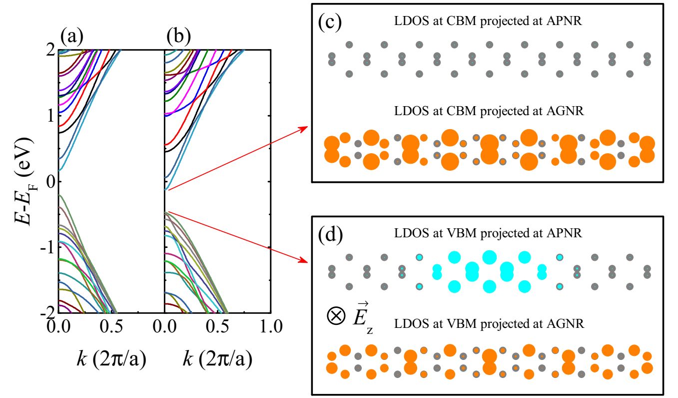

FIG. 6. The band dispersion of 19APNR/25AGNR in the (a) absence and (b) presence of the perpendicular electric field of $|E_z| = 0.1$ V/Å. Local density of states (LDOS) of 19APNR/25AGNR at (c) conduction band minimum (CBM), and (d) valence band maximum (VBM) projected at the layers. The direction of the applied perpendicular electric field is depicted in (d).

ΔT, as shown in Fig. 5. Although the transmission spectra of semiconductor/semiconductor junctions are asymmetrical [see Figs. 4(a) and 4(b)], the thermally induced currents are close to zero or do not exceed several tenths of nanoamperes solely due to the exponential decay of the Fermi distribution function. However, since the band gap of AGNR becomes smaller as the width increases, the thermally induced current in the semiconductor/semiconductor junction gradually increases with the ribbon width. Moreover, we find that the current increases linearly with ΔT. A similar linear behavior of the current-ΔT characteristics has been previously reported in layered materials [63,64].

C. External electric field

As we mentioned in the previous section, by breaking the electron-hole symmetry, it is possible to generate a thermally induced current. A high thermally induced current is anticipated if we enhance the electron-hole asymmetry around the Fermi level. An external electric field can be used to control the p- and n-type doping of the HSs [65] with the possibility to engineer symmetry breaking.

Figures 6(a) and 6(b) show the electronic band dispersion of 19APNR/25AGNR in the absence and presence of a perpendicular electric field, respectively. In the presence of the electric field of 0.1 V/Å along the negative direction of the z axis, the middle of the band gap shifts below the Fermi energy by 0.27 eV, as depicted in Fig. 6(b). Figures 6(c) and 6(d), respectively, correspond to Figs. 3(b) and 3(c) when a perpendicular electric field is applied, which indicates that the electronic state distribution at the CBM remains almost unchanged. In contrast, the electronic states of both layers contribute to the electronic distribution at the VBM. Indeed, upon applying an electric field along the negative direction of the z axis, the bands of 25AGNR become lower in energy, whereas those of 19APNR become higher in energy. Further, by increasing the intensity of the electric field, the uppermost valence band of 19APNR and that of 25AGNR approach together. Up to the electric field of 0.1 V/Å, the band alignment

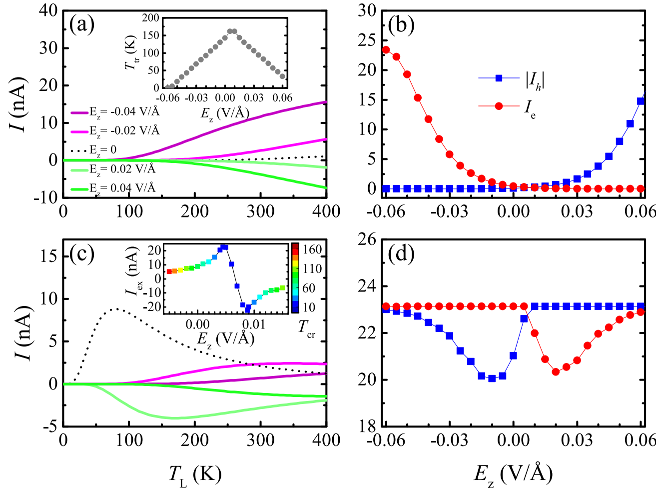

FIG. 7. The thermally induced current of (a) 19APNR/25AGNR and (c) 20APNR/26AGNR vs T_L for different perpendicular electric fields. The threshold temperature for the current of 19APNR/25AGNR as a function of E_z is shown in the inset of (a). The critical point of the current-T_L curve as a function of E_z is shown in the inset of (c). The electron and (the absolute value of) the hole currents of (b) 19APNR/25AGNR and (d) 20APNR/26AGNR vs E_z at room temperature for $\Delta T = 10$ K.

remains type I. The electric field of 0.1 V/Å is a critical value at which a type I-to-II band alignment transition happens. Namely, beyond this value of the electric field, the holes (electrons) are localized in the APNR (AGNR) layer, and an efficient electron-hole separation takes place.

The T_L dependences of the current of 19APNR/25AGNR and 20APNR/26AGNR with $\Delta T = 10$ K for different perpendicular electric fields are shown in Figs. 7(a) and 7(c), respectively. The dotted lines are associated with the current when E_z is set to zero. One can find that the thermally induced current of 19APNR/25AGNR is relatively small. In contrast, the current of 20APNR/26AGNR reaches the maximum value of ∼9 nA at $T_L = 80$ K and decreases to a few nanoamperes at higher temperature, in the absence of any applied field. The figures reveal that both the magnitude of the current and the direction of the current flow can be controlled by the perpendicular electric field. For the depicted current spectra in Fig. 7(a), there is a threshold temperature (T_{tr}), and no current is induced to the 19APNR/25AGNR at low temperatures for the given electric fields. However, variation of T_{tr} vs the applied perpendicular electric field is depicted in the inset of Fig. 7(a), which indicates that the threshold temperature can be reduced even to zero using the perpendicular electric field. Among the depicted curves in Fig. 7(a), under $E_z = -0.04$ V/Å, the magnitude of the current is relatively large (∼12 nA at room temperature), and the threshold temperature is 43 K. It is evident that the current shows a higher value when ΔT is enhanced. For example, below $E_z = -0.04$ V/Å and at $T_L = 300$ K, the calculated current of 19APNR/25AGNR at $\Delta T = 30$ K is ∼3 times higher than that at $\Delta T = 10$ K, which suggests that the current increases with ΔT almost linearly. In general, the thermally induced current of such an armchair-edged semiconductor/semiconductor HS tends to increase as T_L gets larger. Figures 7(b) and 7(d) show the electron and (the absolute value of) hole currents in 19APNR/25AGNR and 20APNR/26AGNR, respectively, as functions of E_z, at room temperature and $\Delta T = 10$ K. According to Fig. 7(b), the electron and hole currents are nearly suppressed by the electric field of $0 < E_z < 0.015$ V/Å, giving rise to a suppressed (or a tiny) net current. Indeed, there is a turning point in the I-E_z characteristics of 19APNR/25AGNR within the range of $0 < E_z < 0.015$ V/Å, where I_e equals I_h. When $E_z \geqslant 0.015$ V/Å, I_e vanishes, while the magnitude of I_h increases with E_z, and a negative current is therefore generated, which shows an increasing behavior (regardless of the sign) over E_z. In contrast, for $E_z \leqslant 0$, since I_e dominates over I_h, a positive net current is created in the system. Moreover, I_e (and of the net current) shows an increasing trend with the increase of the magnitude of the electric field along the negative direction of the z axis. In the case of 20APNR/26AGNR, the threshold temperature is 5 K in the absence of an electric field [Fig. 7(c)], and it vanishes by applying the electric field of $E_z = 0.002$–0.012 V/Å (not shown in the figure). The inset of Fig. 7(c) represents the critical point of the current-T_L curve as a function of the perpendicular electric field in the range of $-0.005 \leqslant E_z \leqslant 0.015$ V/Å. We find that the maximal current of 20APNR/26AGNR, exceeding 20 nA (in both directions), occurs <20 K. As shown in Fig. 7(d), the electron (hole) current of 20APNR/26AGNR remains almost unchanged up (down) to the electric field of 0.005 V/Å (0.007 V/Å). Up to $E_z = 0.006$ V/Å, I_e highly dominates over I_h, and a positive net current is created in the system. In contrast, down to $E_z = 0.006$ V/Å, I_h highly dominates over I_e, and a negative net current is created. Therefore, there is a turning point in the I-E_z characteristic of 20APNR/26AGNR when $E_z = 0.006$ V/Å, where the electron and hole currents cancel each other. However, one can find that the maximal current created at room temperature in 20APNR/26AGNR is as low as a few nanoamperes. We conclude that, for such an armchair-edged semiconductor/metal HS, a significant modulation of the thermally induced current can be obtained by utilizing a perpendicular electric field at low temperatures.

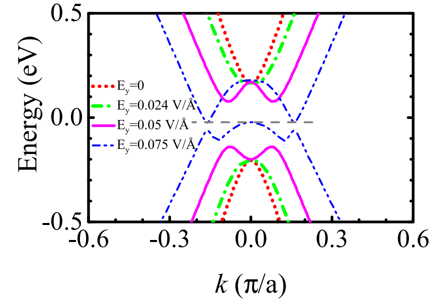

FIG. 8. The evolution of the band edges of 19APNR/25AGNR under a transverse electric field.

Now we consider the effect of the transverse electric field, along the y axis, on the electronic properties of the ribbon. Figure 8 shows the evolution of the band edges of 19APNR/25AGNR under a transverse electric field. As we mentioned earlier, the system has a direct band gap when the applied external electric field is set to zero. Up to the transverse electric field of 0.024 V/Å, the band gap remains

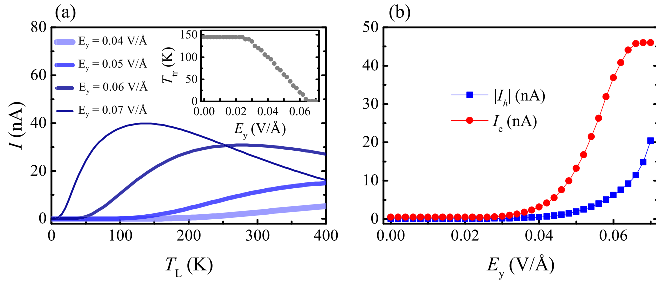

FIG. 9. (a) The thermally induced current of 19APNR/25AGNR as a function of T_L for different transverse electric fields. (b) The electron and (the absolute value of) the hole currents of 19APNR/25AGNR as functions of E_y at room temperature and $\Delta T = 10$ K.

almost unchanged, as shown in the figure. As the electric field increases, the band gap gets smaller and gradually moves away from $k = 0$ toward $2\pi/a$ in the one-dimensional (1D) Brillouin zone. Moreover, the figure shows that the electric field of $E_y = 0.075$ V/Å is the critical electric field at which the band gap closes and the system undergoes a semiconductor-metal phase transition. Furthermore, up to the electric field of 0.07 V/Å, the band gap remains nearly direct (not shown in the figure). When the applied electric field has a value between 0.07 and 0.075 V/Å, a direct-to-indirect band gap transition takes place.

Figure 9(a) shows the current of 19APNR/25AGNR as a function of T_L with $\Delta T = 10$ K for different transverse electric fields. We mentioned earlier that the thermally induced current of 19APNR/25AGNR is relatively small without any external electric field. Figure 9(a) demonstrates that one can increase the current to several tens of nanoamperes using the transverse electric field. In this case, under $E_y = 0.06$ V/Å, the maximal current of ∼30 nA is obtained at the critical value of $T_L = 280$ K, and when $E_y = 0.07$ V/Å is applied, the maximal current of ∼40 nA is created at the critical temperature of $T_L = 140$ K. As expected from the linear variation of the current vs ΔT, when the transverse electric field is set to 0.06 V/Å, the calculated current of 19APNR/25AGNR is ∼90 nA at $T_L = 280$ K and $\Delta T = 30$ K. Moreover, as shown in the inset of the figure, the threshold temperature of the ribbon gets smaller by the transverse electric field and can be reduced to zero. Among the depicted curves in Fig. 9(a), at room temperature, the thermally induced current is more pronounced under $E_y = 0.06$ V/Å (∼30 nA), while at low temperature, the significant values of the current can be generated under $E_y = 0.07$ V/Å (∼40 nA at $T_L = 140$ K). Figure 9(b) shows the electron and (the absolute value of) hole currents in 19APNR/25AGNR as functions of E_y at room temperature and $\Delta T = 10$ K. According to Fig. 9(b), up to the electric field of 0.024 V/Å, the electron and hole currents almost remain unchanged because of the unchanged band gap (see Fig. 8). Beyond this value of the transverse electric field, it is straightforward to see that the higher the intensity of the field, the more I_h (regardless of the sign) dominates over I_e.

IV. SUMMARY AND CONCLUSIONS

In summary, we have investigated the thermally induced current in an APNR/AGNR vdW HS using the TB model and Green's function method. To check the reliability of the TB parametrization, we used the model to calculate the electronic structure of a 2D HS and found good agreement with those from DFT calculations.

We further studied the evolution of the current through a two-probe junction driven by a temperature difference between the leads. We noted that the electronic configuration of the APNR/AGNR vdW HS depends on the width of AGNR, which can be semiconductor/semiconductor or semiconductor/metal. We found that, unlike pristine AGNRs and APNRs, an armchair-edged HS can provide several nanoamperes of thermally induced current even without any external electric field.

We also investigated the effect of perpendicular and transverse electric fields on the electronic features of APNR/AGNR. The results indicate the possibility to induce a band alignment transition from type I to II using a perpendicular electric field on APNR/AGNR. In addition, we found that the system can experience a direct-indirect band gap transition under a transverse electric field. The giant electric-field-induced band modulation leads to a tunable temperature-dependent current. Biasing the APNR/AGNR by an external electric field was demonstrated to enhance the thermally induced current, even up to tens of nanoamperes.

ACKNOWLEDGMENT

Part of this paper was supported by HSE University Basic Research Program.

The authors declare no competing interests.

APPENDIX

According to Fig. 1(a), the supercell of the HS contains 28 atoms. As shown in Fig. 1(b), the atomic sites per unit cell are labeled by P_1, P_2, P_3, …, and P_{12} for phosphorus atoms and C_1, C_2, C_3, …, and C_{16} for carbon atoms. We use a low-energy effective Hamiltonian within the TB model with one π-electron per atom. Hence, the real-space Hamiltonian is a 28×28 matrix described as

$$\mathbf{H} = \sum_{i,j} t_{ij} c_i^\dagger c_j + \mathrm{e}E_z \sum_i z_i c_i^\dagger c_i + \mathrm{e}E_y \sum_i y_i c_i^\dagger c_i, \qquad \text{(A1)}$$

where the summation runs over the lattice sites, and $c_i^\dagger(c_i)$ represents the creation (annihilation) operator of electrons at site i. The first term is the hopping energy, where t_{ij} denotes the hopping parameter between two sites i and j. The second and third terms, involving diagonal elements of the Hamiltonian matrix, describe the potentials caused by the perpendicular and transverse electric fields, respectively, where e is the electron charge, and z_i (y_i) represents the z (y)-coordinate of site i. Here, we provide a detailed representation of the Hamiltonian without any external potential. The hopping parameters of the system are described within a

simplified TB model for the phosphorene layer, including five hopping parameters ($t_1^{\mathrm{p}} = -1.220$ eV, $t_2^{\mathrm{p}} = 3.665$ eV, $t_3^{\mathrm{p}} = -0.205$ eV, $t_4^{\mathrm{p}} = -0.105$ eV, and $t_5^{\mathrm{p}} = -0.055$ eV), and first- and second- neighbor hopping parameters for the graphene layer ($t_1^{\mathrm{c}} = -2.7$ eV and $t_2^{\mathrm{c}} = -0.2$ eV), as shown in Fig. 1(b). The coupling Hamiltonian between the layers is described by the interlayer hopping parameter t^{pc} up to a distance of 4 Å.

The **K**-dependent Hamiltonian on the basis of $(|\mathrm{P}_1\rangle, |\mathrm{P}_2\rangle, |\mathrm{P}_3\rangle, \ldots, |\mathrm{P}_{12}\rangle, |\mathrm{C}_1\rangle, |\mathrm{C}_2\rangle, |\mathrm{C}_3\rangle, \ldots, |\mathrm{C}_{16}\rangle)^{\mathrm{T}}$ is given by

$$\mathbf{H}_{\mathbf{K}} = \begin{bmatrix} \mathbf{H}_{\mathbf{K}}^{\mathrm{P}} & \mathbf{H}_{\mathbf{K}}^{\mathrm{PG}} \\ \mathbf{H}_{\mathbf{K}}^{\mathrm{PG}\dagger} & \mathbf{H}_{\mathbf{K}}^{\mathrm{G}} \end{bmatrix}, \tag{A2}$$

where $\mathbf{H}_{\mathbf{K}}^{\mathrm{P}}$, $\mathbf{H}_{\mathbf{K}}^{\mathrm{G}}$, and $\mathbf{H}_{\mathbf{K}}^{\mathrm{PG}}$ denote the **K**-dependent Hamiltonians of phosphorene (a 12×12 matrix), graphene (a 16×16 matrix), and coupling between the layers (a 12×16 matrix), respectively, explicitly evaluated as

$$\boldsymbol{H}_{\mathbf{K}}^{\mathrm{P}} = \begin{bmatrix}
0 & A_{\mathbf{K}}^{\mathrm{P}} & B_{\mathbf{K}}^{\mathrm{P}} & C_{\mathbf{K}}^{\mathrm{P}} & 0 & 0 & 0 & 0 & 0 & 0 & D_{\mathbf{K}}^{\mathrm{P}} & E_{\mathbf{K}}^{\mathrm{P}} \\
A_{\mathbf{K}}^{\mathrm{P}*} & 0 & C_{\mathbf{K}}^{\mathrm{P}*} & B_{\mathbf{K}}^{\mathrm{P}*} & 0 & 0 & 0 & 0 & 0 & 0 & F_{\mathbf{K}}^{\mathrm{P}} & G_{\mathbf{K}}^{\mathrm{P}} \\
B_{\mathbf{K}}^{\mathrm{P}*} & C_{\mathbf{K}}^{\mathrm{P}} & 0 & H_{\mathbf{K}}^{\mathrm{P}} & B_{\mathbf{K}}^{\mathrm{P}*} & C_{\mathbf{K}}^{\mathrm{P}} & 0 & 0 & 0 & 0 & 0 & 0 \\
C_{\mathbf{K}}^{\mathrm{P}*} & B_{\mathbf{K}}^{\mathrm{P}} & H_{\mathbf{K}}^{\mathrm{P}*} & 0 & C_{\mathbf{K}}^{\mathrm{P}*} & B_{\mathbf{K}}^{\mathrm{P}} & 0 & 0 & 0 & 0 & 0 & 0 \\
0 & 0 & B_{\mathbf{K}}^{\mathrm{P}} & C_{\mathbf{K}}^{\mathrm{P}} & 0 & A_{\mathbf{K}}^{\mathrm{P}} & B_{\mathbf{K}}^{\mathrm{P}} & C_{\mathbf{K}}^{\mathrm{P}} & 0 & 0 & 0 & 0 \\
0 & 0 & C_{\mathbf{K}}^{\mathrm{P}*} & B_{\mathbf{K}}^{\mathrm{P}*} & A_{\mathbf{K}}^{\mathrm{P}*} & 0 & C_{\mathbf{K}}^{\mathrm{P}*} & B_{\mathbf{K}}^{\mathrm{P}*} & 0 & 0 & 0 & 0 \\
0 & 0 & 0 & 0 & B_{\mathbf{K}}^{\mathrm{P}*} & C_{\mathbf{K}}^{\mathrm{P}} & 0 & H_{\mathbf{K}}^{\mathrm{P}} & B_{\mathbf{K}}^{\mathrm{P}*} & C_{\mathbf{K}}^{\mathrm{P}} & 0 & 0 \\
0 & 0 & 0 & 0 & C_{\mathbf{K}}^{\mathrm{P}*} & B_{\mathbf{K}}^{\mathrm{P}} & H_{\mathbf{K}}^{\mathrm{P}*} & 0 & C_{\mathbf{K}}^{\mathrm{P}*} & B_{\mathbf{K}}^{\mathrm{P}} & 0 & 0 \\
0 & 0 & 0 & 0 & 0 & 0 & B_{\mathbf{K}}^{\mathrm{P}} & C_{\mathbf{K}}^{\mathrm{P}} & 0 & A_{\mathbf{K}}^{\mathrm{P}} & B_{\mathbf{K}}^{\mathrm{P}} & C_{\mathbf{K}}^{\mathrm{P}} \\
0 & 0 & 0 & 0 & 0 & 0 & C_{\mathbf{K}}^{\mathrm{P}*} & B_{\mathbf{K}}^{\mathrm{P}*} & A_{\mathbf{K}}^{\mathrm{P}*} & 0 & C_{\mathbf{K}}^{\mathrm{P}*} & B_{\mathbf{K}}^{\mathrm{P}*} \\
D_{\mathbf{K}}^{\mathrm{P}*} & F_{\mathbf{K}}^{\mathrm{P}*} & 0 & 0 & 0 & 0 & 0 & 0 & B_{\mathbf{K}}^{\mathrm{P}*} & C_{\mathbf{K}}^{\mathrm{P}} & 0 & H_{\mathbf{K}}^{\mathrm{P}} \\
E_{\mathbf{K}}^{\mathrm{P}*} & G_{\mathbf{K}}^{\mathrm{P}*} & 0 & 0 & 0 & 0 & 0 & 0 & C_{\mathbf{K}}^{\mathrm{P}*} & B_{\mathbf{K}}^{\mathrm{P}} & H_{\mathbf{K}}^{\mathrm{P}*} & 0
\end{bmatrix}_{12\times 12} \tag{A3}$$

$$\boldsymbol{H}_{\mathbf{K}}^{\mathrm{G}} = \begin{bmatrix}
0 & A_{\mathbf{K}}^{\mathrm{G}} & t_1^C & B_{\mathbf{K}}^{\mathrm{G}} & t_2^C & 0 & 0 & 0 & 0 & 0 & 0 & 0 & C_{\mathbf{K}}^{\mathrm{G}} & 0 & D_{\mathbf{K}}^{\mathrm{G}} & E_{\mathbf{K}}^{\mathrm{G}} \\
A_{\mathbf{K}}^{\mathrm{G}*} & 0 & B_{\mathbf{K}}^{\mathrm{G}*} & t_1^C & 0 & t_2^C & 0 & 0 & 0 & 0 & 0 & 0 & 0 & C_{\mathbf{K}}^{\mathrm{G}} & F_{\mathbf{K}}^{\mathrm{G}} & D_{\mathbf{K}}^{\mathrm{G}} \\
t_1^C & B_{\mathbf{K}}^{\mathrm{G}} & 0 & t_1^C & t_1^C & B_{\mathbf{K}}^{\mathrm{G}} & t_2^C & 0 & 0 & 0 & 0 & 0 & 0 & 0 & C_{\mathbf{K}}^{\mathrm{G}} & 0 \\
B_{\mathbf{K}}^{\mathrm{G}*} & t_1^C & t_1^C & 0 & B_{\mathbf{K}}^{\mathrm{G}*} & t_1^C & 0 & t_2^C & 0 & 0 & 0 & 0 & 0 & 0 & 0 & C_{\mathbf{K}}^{\mathrm{G}} \\
t_2^C & 0 & t_1^C & B_{\mathbf{K}}^{\mathrm{G}} & 0 & A_{\mathbf{K}}^{\mathrm{G}} & t_1^C & B_{\mathbf{K}}^{\mathrm{G}} & t_2^C & 0 & 0 & 0 & 0 & 0 & 0 & 0 \\
0 & t_2^C & B_{\mathbf{K}}^{\mathrm{G}*} & t_1^C & A_{\mathbf{K}}^{\mathrm{G}*} & 0 & B_{\mathbf{K}}^{\mathrm{G}*} & t_1^C & 0 & t_2^C & 0 & 0 & 0 & 0 & 0 & 0 \\
0 & 0 & t_2^C & 0 & t_1^C & B_{\mathbf{K}}^{\mathrm{G}} & 0 & t_1^C & t_1^C & B_{\mathbf{K}}^{\mathrm{G}} & t_2^C & 0 & 0 & 0 & 0 & 0 \\
0 & 0 & 0 & t_2^C & B_{\mathbf{K}}^{\mathrm{G}*} & t_1^C & t_1^C & 0 & B_{\mathbf{K}}^{\mathrm{G}*} & t_1^C & 0 & t_2^C & 0 & 0 & 0 & 0 \\
0 & 0 & 0 & 0 & t_2^C & 0 & t_1^C & B_{\mathbf{K}}^{\mathrm{G}} & 0 & A_{\mathbf{K}}^{\mathrm{G}} & t_1^C & B_{\mathbf{K}}^{\mathrm{G}} & t_2^C & 0 & 0 & 0 \\
0 & 0 & 0 & 0 & 0 & t_2^C & B_{\mathbf{K}}^{\mathrm{G}*} & t_1^C & A_{\mathbf{K}}^{\mathrm{G}*} & 0 & B_{\mathbf{K}}^{\mathrm{G}*} & t_1^C & 0 & t_2^C & 0 & 0 \\
0 & 0 & 0 & 0 & 0 & 0 & t_2^C & 0 & t_1^C & B_{\mathbf{K}}^{\mathrm{G}} & 0 & t_1^C & t_1^C & B_{\mathbf{K}}^{\mathrm{G}} & t_2^C & 0 \\
0 & 0 & 0 & 0 & 0 & 0 & 0 & t_2^C & B_{\mathbf{K}}^{\mathrm{G}*} & t_1^C & t_1^C & 0 & B_{\mathbf{K}}^{\mathrm{G}*} & t_1^C & 0 & t_2^C \\
C_{\mathbf{K}}^{\mathrm{G}*} & 0 & 0 & 0 & 0 & 0 & 0 & 0 & t_2^C & 0 & t_1^C & B_{\mathbf{K}}^{\mathrm{G}} & 0 & A_{\mathbf{K}}^{\mathrm{G}} & t_1^C & B_{\mathbf{K}}^{\mathrm{G}} \\
0 & C_{\mathbf{K}}^{\mathrm{G}*} & 0 & 0 & 0 & 0 & 0 & 0 & 0 & t_2^C & B_{\mathbf{K}}^{\mathrm{G}*} & t_1^C & A_{\mathbf{K}}^{\mathrm{G}*} & 0 & B_{\mathbf{K}}^{\mathrm{G}*} & t_1^C \\
D_{\mathbf{K}}^{\mathrm{G}*} & F_{\mathbf{K}}^{\mathrm{G}*} & C_{\mathbf{K}}^{\mathrm{G}*} & 0 & 0 & 0 & 0 & 0 & 0 & 0 & t_2^C & 0 & t_1^C & B_{\mathbf{K}}^{\mathrm{G}} & 0 & t_1^C \\
E_{\mathbf{K}}^{\mathrm{G}*} & D_{\mathbf{K}}^{\mathrm{G}*} & 0 & C_{\mathbf{K}}^{\mathrm{G}*} & 0 & 0 & 0 & 0 & 0 & 0 & 0 & t_2^C & B_{\mathbf{K}}^{\mathrm{G}*} & t_1^C & t_1^C & 0
\end{bmatrix}_{16\times 16} \tag{A4}$$

$$
\boldsymbol{H}_{\mathbf{K}}^{\mathrm{PG}} = \begin{bmatrix}
t^{pc} & A_K^{PG} & t^{pc} & A_K^{PG} & t^{pc} & 0 & 0 & 0 & 0 & 0 & 0 & 0 & 0 & 0 & 0 & 0 \\
0 & 0 & 0 & 0 & 0 & 0 & 0 & 0 & 0 & 0 & 0 & 0 & 0 & 0 & 0 & 0 \\
0 & 0 & t^{pc} & t^{pc} & t^{pc} & t^{pc} & t^{pc} & t^{pc} & 0 & 0 & 0 & 0 & 0 & 0 & 0 & 0 \\
0 & 0 & 0 & 0 & 0 & 0 & 0 & 0 & 0 & 0 & 0 & 0 & 0 & 0 & 0 & 0 \\
0 & 0 & 0 & 0 & t^{pc} & A_K^{PG} & t^{pc} & A_K^{PG} & t^{pc} & A_K^{PG} & 0 & 0 & 0 & 0 & 0 & 0 \\
0 & 0 & 0 & 0 & 0 & 0 & 0 & 0 & 0 & 0 & 0 & 0 & 0 & 0 & 0 & 0 \\
0 & 0 & 0 & 0 & 0 & 0 & t^{pc} & t^{pc} & t^{pc} & t^{pc} & t^{pc} & t^{pc} & 0 & 0 & 0 & 0 \\
0 & 0 & 0 & 0 & 0 & 0 & 0 & 0 & 0 & 0 & 0 & 0 & 0 & 0 & 0 & 0 \\
0 & 0 & 0 & 0 & 0 & 0 & 0 & 0 & t^{pc} & 0 & t^{pc} & A_K^{PG} & t^{pc} & A_K^{PG} & t^{pc} & 0 \\
0 & 0 & 0 & 0 & 0 & 0 & 0 & 0 & 0 & 0 & 0 & 0 & 0 & 0 & 0 & 0 \\
B_K^{PG} & 0 & 0 & 0 & 0 & 0 & 0 & 0 & 0 & 0 & 0 & 0 & t^{pc} & 0 & t^{pc} & t^{pc} \\
0 & 0 & 0 & 0 & 0 & 0 & 0 & 0 & 0 & 0 & 0 & 0 & 0 & 0 & 0 & 0
\end{bmatrix}_{12\times 16} \tag{A5}
$$

whose elements are given by

$$
\begin{aligned}
A_{\mathbf{K}}^{\mathrm{P}} &= t_5^{\mathrm{p}} + t_2^{\mathrm{p}}\exp(-\mathrm{i}k_a),\\
B_{\mathbf{K}}^{\mathrm{P}} &= t_1^{\mathrm{p}} + t_3^{\mathrm{p}}\exp(-\mathrm{i}k_a),\\
C_{\mathbf{K}}^{\mathrm{P}} &= 2t_4^{\mathrm{p}}\exp\left(-\frac{\mathrm{i}k_a}{2}\right)\cos\left(\frac{k_a}{2}\right),\\
D_{\mathbf{K}}^{\mathrm{P}} &= t_1^{\mathrm{p}}\exp(-\mathrm{i}k_b) + t_3^{\mathrm{p}}\exp[-\mathrm{i}(k_a+k_b)],\\
E_{\mathbf{K}}^{\mathrm{P}} &= 2t_4^{\mathrm{p}}\exp\left(-\frac{\mathrm{i}k_a}{2}\right)\exp(-\mathrm{i}k_b)\cos\left(\frac{k_a}{2}\right),\\
F_{\mathbf{K}}^{\mathrm{P}} &= 2t_4^{\mathrm{p}}\exp\left(\frac{\mathrm{i}k_a}{2}\right)\exp(-\mathrm{i}k_b)\cos\left(\frac{k_a}{2}\right),\\
G_{\mathbf{K}}^{\mathrm{P}} &= t_1^{\mathrm{p}}\exp(-\mathrm{i}k_b) + t_3^{\mathrm{p}}\exp[\mathrm{i}(k_a-k_b)],\\
H_{\mathbf{K}}^{\mathrm{P}} &= t_2^{\mathrm{p}} + t_5^{\mathrm{p}}\exp(-\mathrm{i}k_a),\\
A_{\mathbf{K}}^{\mathrm{G}} &= t_1^{\mathrm{c}}\exp(-\mathrm{i}k_a),\\
B_{\mathbf{K}}^{\mathrm{G}} &= 2t_2^{\mathrm{c}}\exp\left(-\frac{\mathrm{i}k_a}{2}\right)\cos\left(\frac{k_a}{2}\right),\\
C_{\mathbf{K}}^{\mathrm{G}} &= t_2^{\mathrm{c}}\exp(-\mathrm{i}k_b),\\
D_{\mathbf{K}}^{\mathrm{G}} &= t_1^{\mathrm{c}}\exp(-\mathrm{i}k_b),\\
E_{\mathbf{K}}^{\mathrm{G}} &= 2t_2^{\mathrm{c}}\exp\left(-\frac{\mathrm{i}k_a}{2}\right)\exp(-\mathrm{i}k_b)\cos\left(\frac{k_a}{2}\right),\\
F_{\mathbf{K}}^{\mathrm{G}} &= 2t_2^{\mathrm{c}}\exp\left(\frac{\mathrm{i}k_a}{2}\right)\exp(-\mathrm{i}k_b)\cos\left(\frac{k_a}{2}\right),\\
A_{\mathbf{K}}^{\mathrm{PG}} &= t^{\mathrm{pc}}\exp(-\mathrm{i}k_a),\\
B_{\mathbf{K}}^{\mathrm{PG}} &= t^{\mathrm{pc}}\exp(\mathrm{i}k_b),
\end{aligned} \tag{A6}
$$

where $k_a = \mathbf{K}\cdot\mathbf{a}$ and $k_b = \mathbf{K}\cdot\mathbf{b}$. Here, $\mathbf{a} = a\hat{\mathbf{x}}$ and $\mathbf{b} = b\hat{\mathbf{y}}$, where $a = 4.43$ Å and $b = 9.81$ Å are the lattice constants. Diagonalizing the Hamiltonian matrix, we obtain the energy spectrum.

[1] K. S. Novoselov, A. K. Geim, S. V. Morozov, D. Jiang, Y. Zhang, S. V. Dubonos, I. V. Grigorieva, and A. A. Firsov, Electric field effect in atomically thin carbon films, Science. **306**, 666 (2004).

[2] K. S. Novoselov, D. Jiang, F. Schedin, T. Booth, V. Khotkevich, S. Morozov, and A. K. Geim, Two-dimensional atomic crystals, Proc. Natl. Acad. Sci. **102**, 10451 (2005).

[3] K. F. Mak, C. Lee, J. Hone, J. Shan, and T. F. Heinz, Atomically thin MoS_2: A new direct-gap semiconductor, Phys. Rev. Lett. **105**, 136805 (2010).

[4] H. Liu, A. T. Neal, Z. Zhu, Z. Luo, X. Xu, D. Tománek, and P. D. Ye, Phosphorene: An unexplored 2D semiconductor with a high hole mobility, ACS Nano. **8**, 4033 (2014).

[5] X. Blase, A. Rubio, S. G. Louie, and M. L. Cohen, Quasiparticle band structure of bulk hexagonal boron nitride and related systems, Phys. Rev. B. **51**, 6868 (1995).

[6] B. Mortazavi, X. Zhuang, and T. Rabczuk, A first-principles study on the physical properties of two-dimensional Nb_3Cl_8, Nb_3Br_8 and Nb_3I_8, Appl. Phys. A. **128**, 934 (2022).

[7] Y. Zhang, Y.-W. Tan, H. L. Stormer, and P. Kim, Experimental observation of the quantum Hall effect and Berry's phase in graphene, Nature (London). **438**, 201 (2005).

[8] P. R. Wallace, The band theory of graphite, Phys. Rev. **71**, 622 (1947).

[9] S. Morozov, K. Novoselov, M. Katsnelson, F. Schedin, D. C. Elias, J. A. Jaszczak, and A. K. Geim, Giant intrinsic carrier mobilities in graphene and its bilayer, Phys. Rev. Lett. **100**, 016602 (2008).

[10] A. C. Neto, F. Guinea, N. M. Peres, K. S. Novoselov, and A. K. Geim, The electronic properties of graphene, Rev. Mod. Phys. **81**, 109 (2009).

[11] M. I. Katsnelson, K. S. Novoselov, and A. K. Geim, Chiral tunnelling and the Klein paradox in graphene, Nat. Phys. **2**, 620 (2006).
[12] K. Nakada, M. Fujita, G. Dresselhaus, and M. S. Dresselhaus, Edge state in graphene ribbons: Nanometer size effect and edge shape dependence, Phys. Rev. B. **54**, 17954 (1996).
[13] M. Fujita, K. Wakabayashi, K. Nakada, and K. Kusakabe, Peculiar localized state at zigzag graphite edge, J. Phys. Soc. Jpn. **65**, 1920 (1996).
[14] K. Wakabayashi, Electronic transport properties of nanographite ribbon junctions, Phys. Rev. B. **64**, 125428 (2001).
[15] M. Ezawa, Peculiar width dependence of the electronic properties of carbon nanoribbons, Phys. Rev. B. **73**, 045432 (2006).
[16] A. Castellanos-Gomez, L. Vicarelli, E. Prada, J. O. Island, K. Narasimha-Acharya, S. I. Blanter, D. J. Groenendijk, M. Buscema, G. A. Steele, J. V. Alvarez *et al.*, Isolation and characterization of few-layer black phosphorus, 2D Mater. **1**, 025001 (2014).
[17] W. Lu, H. Nan, J. Hong, Y. Chen, C. Zhu, Z. Liang, X. Ma, Z. Ni, C. Jin, and Z. Zhang, Plasma-assisted fabrication of monolayer phosphorene and its Raman characterization, Nano Res. **7**, 853 (2014).
[18] R. W. Keyes, The electrical properties of black phosphorus, Phys. Rev. **92**, 580 (1953).
[19] R. B. Jacobs, Phosphorus at high temperatures and pressures, J. Chem. Phys. **5**, 945 (1937).
[20] Z. Zhu and D. Tománek, Semiconducting layered blue phosphorus: A computational study, Phys. Rev. Lett. **112**, 176802 (2014).
[21] P. Bridgman, Further note on black phosphorus, J. Am. Chem. Soc. **38**, 609 (1916).
[22] A. Morita, Semiconducting black phosphorus, Appl. Phys. A. **39**, 227 (1986).
[23] A. Rodin, A. Carvalho, and A. C. Neto, Strain-induced gap modification in black phosphorus, Phys. Rev. Lett. **112**, 176801 (2014).
[24] F. Xia, H. Wang, and Y. Jia, Rediscovering black phosphorus as an anisotropic layered material for optoelectronics and electronics, Nat. Commun. **5**, 4458 (2014).
[25] Y. Takao, H. Asahina, and A. Morita, Electronic structure of black phosphorus in tight binding approach, J. Phys. Soc. Jpn. **50**, 3362 (1981).
[26] V. Tran, R. Soklaski, Y. Liang, and L. Yang, Layer-controlled band gap and anisotropic excitons in few-layer black phosphorus, Phys. Rev. B **89**, 235319 (2014).
[27] L. Li, J. Kim, C. Jin, G. J. Ye, D. Y. Qiu, F. H. da Jornada, Z. Shi, L. Chen, Z. Zhang, F. Yang *et al.*, Direct observation of the layer-dependent electronic structure in phosphorene, Nat. Nanotechnol. **12**, 21 (2017).
[28] L. Li, Y. Yu, G. J. Ye, Q. Ge, X. Ou, H. Wu, D. Feng, X. H. Chen, and Y. Zhang, Black phosphorus field-effect transistors, Nat. Nanotechnol. **9**, 372 (2014).
[29] Y. Betancur-Ocampo, F. Leyvraz, and T. Stegmann, Electron optics in phosphorene *pn* junctions: Negative reflection and anti-super-Klein tunneling, Nano Lett. **19**, 7760 (2019).
[30] E. S. Kadantsev and P. Hawrylak, Electronic structure of a single MoS_2 monolayer, Solid State Commun. **152**, 909 (2012).
[31] X. Liu, J. D. Wood, K.-S. Chen, E. Cho, and M. C. Hersam, *In situ* thermal decomposition of exfoliated two-dimensional black phosphorus, J. Phys. Chem. Lett. **6**, 773 (2015).
[32] J. O. Island, G. A. Steele, H. S. van der Zant, and A. Castellanos-Gomez, Environmental instability of few-layer black phosphorus, 2D Materials. **2**, 011002 (2015).
[33] A. K. Geim and I. V. Grigorieva, van der Waals heterostructures, Nature (London). **499**, 419 (2013).
[34] M.-H. Chiu, C. Zhang, H.-W. Shiu, C.-P. Chuu, C.-H. Chen, C.-Y. S. Chang, C.-H. Chen, M.-Y. Chou, C.-K. Shih, and L.-J. Li, Determination of band alignment in the single-layer MoS_2/WSe_2 heterojunction, Nat. Commun. **6**, 7666 (2015).
[35] C. Q. Nguyen, Y. S. Ang, S.-T. Nguyen, N. V. Hoang, N. M. Hung, and C. V. Nguyen, Tunable type-II band alignment and electronic structure of $C_3N_4/MoSi_2N_4$ heterostructure: Interlayer coupling and electric field, Phys. Rev. B. **105**, 045303 (2022).
[36] J. E. Padilha, A. Fazzio, and A. J. da Silva, van der Waals heterostructure of phosphorene and graphene: Tuning the Schottky barrier and doping by electrostatic gating, Phys. Rev. Lett. **114**, 066803 (2015).
[37] J. Dai and X. C. Zeng, Bilayer phosphorene: Effect of stacking order on bandgap and its potential applications in thin-film solar cells, J. Phys. Chem. Lett. **5**, 1289 (2014).
[38] A. Avsar, I. J. Vera-Marun, J. Y. Tan, K. Watanabe, T. Taniguchi, A. H. Castro Neto, and B. Özyilmaz, Air-stable transport in graphene-contacted, fully encapsulated ultrathin black phosphorus-based field-effect transistors, ACS Nano. **9**, 4138 (2015).
[39] X. Xiong, M. Huang, B. Hu, X. Li, F. Liu, S. Li, J. Song, and Y. Wu, A transverse tunnelling field-effect transistor made from a van der Waals heterostructure, Nat. Electron. **3**, 106 (2020).
[40] Y. Cai, G. Zhang, and Y.-W. Zhang, Electronic properties of phosphorene/graphene and phosphorene/hexagonal boron nitride heterostructures, J. Phys. Chem. C **119**, 13929 (2015).
[41] M. Zeng, Y. Feng, and G. Liang, Thermally induced currents in graphene-based heterostructure, Appl. Phys. Lett. **99**, 123114 (2011).
[42] R. Hu, Z. Zhou, C. Sheng, L. Wang, J. Liu, S. Han, and H. J. Liu, Surprisingly good thermoelectric performance of a black phosphorus/blue phosphorus van der Waals heterostructure, Phys. Chem. Chem. Phys. **22**, 22390 (2020).
[43] J. Zhang, H. Liu, L. Cheng, J. Wei, J. Liang, D. Fan, J. Shi, X. F. Tang, and Q. J. Zhang, Phosphorene nanoribbon as a promising candidate for thermoelectric applications, Sci. Rep. **4**, 6452 (2014).
[44] Y. Ouyang and J. Guo, A theoretical study on thermoelectric properties of graphene nanoribbons, Appl. Phys. Lett. **94**, 263107 (2009).
[45] F. M. Borojeni, E. T. Sisakht, F. Fazileh, and F. Peeters, Enhanced thermoelectric properties in phosphorene nanorings, Phys. Rev. B. **108**, 035425 (2023).
[46] G. Gui, J. Li, and J. Zhong, Band structure engineering of graphene by strain: First-principles calculations, Phys. Rev. B **78**, 075435 (2008).
[47] A. N. Rudenko and M. I. Katsnelson, Quasiparticle band structure and tight-binding model for single-and bilayer black phosphorus, Phys. Rev. B **89**, 201408 (2014).
[48] Y. Hancock, A. Uppstu, K. Saloriutta, A. Harju, and M. J. Puska, Generalized tight-binding transport model for graphene nanoribbon-based systems, Phys. Rev. B. **81**, 245402 (2010).

[49] M. Qasemnazhand, F. Khoeini, and S. Shekarforoush, Electronic transport properties in the stable phase of a cumulene/B_7/cumulene molecular bridge investigated using density functional theory and a tight-binding method, New J. Chem. **43**, 16515 (2019).
[50] S. Datta, *Electronic Transport in Mesoscopic Systems* (Cambridge University Press, Cambridge, 1997).
[51] F. Khoeini, F. Khoeini, and A. Shokri, Peculiar transport properties in Z-shaped graphene nanoribbons: A nanoscale NOR gate, Thin Solid Films. **548**, 443 (2013).
[52] M. L. Sancho, J. L. Sancho, and J. Rubio, Quick iterative scheme for the calculation of transfer matrices: Application to Mo(100), J. Phys. F Met. Phys. **14**, 1205 (1984).
[53] M. L. Sancho, J. L. Sancho, J. L. Sancho, and J. Rubio, Highly convergent schemes for the calculation of bulk and surface Green functions, J. Phys. F Met. Phys. **15**, 851 (1985).
[54] F. Khoeini, A. A. Shokri, and F. Khoeini, Electronic transport through superlattice-graphene nanoribbons, Eur. Phys. J. B **75**, 505 (2010).
[55] S. Datta, *Quantum Transport: Atom to Transistor* (Cambridge University Press, Cambridge, 2005).
[56] M. Mahdavifar and F. Khoeini, Topological and transport properties of graphene-based nanojunctions subjected to a magnetic field, Nanotechnology. **31**, 025701 (2019).
[57] F. Khoeini, K. Shakouri, and F. Peeters, Peculiar half-metallic state in zigzag nanoribbons of MoS_2: Spin filtering, Phys. Rev. B **94**, 125412 (2016).
[58] X.-R. Hu, J.-M. Zheng, and Z.-Y. Ren, Strong interlayer coupling in phosphorene/graphene van der Waals heterostructure: A first-principles investigation, Front. Phys. **13**, 137302 (2018).
[59] E. T. Sisakht, M. H. Zare, and F. Fazileh, Scaling laws of band gaps of phosphorene nanoribbons: A tight-binding calculation, Phys. Rev. B **91**, 085409 (2015).
[60] D.-D. Wu, Q.-B. Liu, H.-H. Fu, and R. Wu, How to realize a spin-dependent Seebeck diode effect in metallic zigzag γ-graphyne nanoribbons? Nanoscale **9**, 18334 (2017).
[61] T. Thakur and B. Szafran, Wigner molecules in phosphorene quantum dots, Phys. Rev. B. **106**, 205304 (2022).
[62] M. Mahdavifar, S. Shekarforoush, and F. Khoeini, Tunable electronic properties and electric-field-induced phase transition in phosphorene/graphene heterostructures, J. Phys. D Appl. Phys. **54**, 095108 (2020).
[63] L. Zhu, F. Zou, G. Gao, and K. Yao, Spin-dependent thermoelectric effects in Fe-C_6 doped monolayer MoS_2, Sci. Rep. **7**, 497 (2017).
[64] Y. Ni, K. Yao, H. Fu, G. Gao, S. Zhu, and S. Wang, Spin Seebeck effect and thermal colossal magnetoresistance in graphene nanoribbon heterojunction, Sci. Rep. **3**, 1380 (2013).
[65] J. E. Padilha, R. H. Miwa, A. J. da Silva, and A. Fazzio, Two-dimensional van der Waals *pn* junction of InSe/phosphorene, Phys. Rev. B. **95**, 195143 (2017).